

Ram-pressure stripping caught in action in a forming galaxy cluster 3 billion years after the Big Bang

Ke Xu^{1,2}, Tao Wang^{1,2*}, Emanuele Daddi³, David Elbaz³,
Hanwen Sun^{1,2}, Longyue Chen^{1,2}, Raphael Gobat⁴, Anita Zanella⁵,
Daizhong Liu⁶, Mengyuan Xiao⁷, Renyue Cen⁸, Tadayuki Kodama⁹,
Kotaro Kohno^{10,11}, Tiancheng Yang^{1,2}, Zhi-Yu Zhang^{1,2},
Luwenjia Zhou^{1,2}, Francesco Valentino^{12,13,14}

¹School of Astronomy and Space Science, Nanjing University, Nanjing, Jiangsu 210093, China.

²Key Laboratory of Modern Astronomy and Astrophysics, Nanjing University, Ministry of Education, Nanjing 210093, China.

³AIM, CEA, CNRS, Université Paris-Saclay, Université Paris Diderot, Sorbonne Paris Cité, F-91191 Gif-sur-Yvette, France.

⁴Instituto de Física, Pontificia Universidad Católica de Valparaíso, Casilla 4059, Valparaíso, Chile.

⁵Istituto Nazionale di Astrofisica (INAF), Vicolo dell'Osservatorio 5, I-35122 Padova, Italy.

⁶Purple Mountain Observatory, Chinese Academy of Sciences, 10 Yuanhua Road, Nanjing 210023, China.

⁷Department of Astronomy, University of Geneva, Chemin Pegasi 51, 1290 Versoix, Switzerland.

⁸Center for Cosmology and Computational Astrophysics, Institute for Advanced Study in Physics, and Institute of Astronomy, School of Physics, Zhejiang University, Hangzhou 310027, China.

⁹Astronomical Institute, Tohoku University, Aramaki, Aoba-ku, Sendai 980-8578, Japan.

¹⁰Institute of Astronomy, School of Science, The University of Tokyo, 2-21-1

Osawa, Mitaka, Tokyo 181-0015, Japan.

¹¹Research Center for the Early Universe, School of Science,
The University of Tokyo, 7-3-1 Hongo, Bunkyo, Tokyo 113-0033, Japan.

¹²Cosmic Dawn Center (DAWN), Denmark.

¹³Niels Bohr Institute, University of Copenhagen, Jagtvej 128, DK-2200 Copenhagen N, Denmark.

¹⁴European Southern Observatory, Karl-Schwarzschild-Str. 2, D-85748 Garching bei Munchen, Germany.

*Corresponding author. Email: taowang@nju.edu.cn

Galaxy clusters in the local Universe are dominated by massive quiescent galaxies with old ages, formed at high redshifts. It is debated whether their quenching is driven by internal processes or environmental effects, which has been challenging due to the lack of observations during their peak formation epoch. Here we report clear evidence from ALMA of extended and elongated gas tails in nine galaxies in a forming cluster at $z = 2.51$. The distinct gas distribution compared to the stellar emission probed by JWST, which is rather isolated without signatures of mergers or interactions, provides evidence of ram-pressure stripping (RPS). This represents the most distant confirmed case of RPS, highlighting the critical role of environmental effects in gas removal at high redshifts, an often overlooked quenching pathway.

Direct evidence of the impact of environmental effects on cluster galaxies during their major formation epoch, $z \sim 2 - 4$, has been so far lacking. Most structures discovered at these epochs are either too young and extended with their halo masses far below typical clusters, or already pretty mature with the presence of a dominant population of quiescent galaxies. Recently, a novel type of structures has been discovered at $z \gtrsim 2$ (*I*), exhibiting a high galaxy density (and halo mass) in the core, yet most of their member galaxies remain star-forming. Among these structures, CLJ1001 (2, 3) at $z = 2.51$ with a total mass close to a mature cluster ($M \sim 0.5 - 1 \times 10^{14} M_{\odot}$) (2) could serve as a crucial bridge between more extended protoclusters and fully formed galaxy clusters. The abundance of massive star-forming galaxies (SFGs) in a cluster-like environment makes CLJ1001 an ideal laboratory to investigate whether and how the dense environment affects

massive galaxy formation.

CLJ1001 harbors 14 SFGs with $\log(M_{\star}/M_{\odot}) > 10.5$ within the central 340 kpc, most of which are believed to soon transition into quiescent galaxies, as evidenced from their low gas fraction (4), compact sizes (5), and a top-heavy galaxy stellar mass function (6). In order to probe the role of dense environments in the evolution of these massive cluster SFGs, extensive multi-wavelength observations (2, 4, 7) have been conducted (8). In particular, the CO(3-2) observations from ALMA, combined with high-resolution JWST/NIRCam imaging from the COSMOS-Web program (9), enable studies of the spatial distribution of both molecular gas and stars, which are among the most sensitive probes of various environmental effects.

Galaxies exhibiting disturbed gas morphology

The CO(3-2) observations cover member galaxies in CLJ1001 both in the center and in the outskirts, up to twice the virial radius (R_{vir}), with the resolution of $1.09'' \times 0.98''$ (and $1.02'' \times 0.93''$ for the lower single pointing, corresponding to the physical scale of ~ 8 kpc at $z = 2.51$). In total, 20 member galaxies are well detected in CO(3-2) (information summarized in table S1). The spatial distributions of these CO(3-2)-detected members within CLJ1001 are shown in Fig. 1.

The reduced JWST/NIRCam imaging (6) represents one of the first rest-frame near-infrared observation of cluster galaxies at $z > 2$ and covers most areas of CLJ1001 with four exposures in four filters (F115W, F150W, F277W and F444W), reaching $0.14''$ spatial resolution in F444W and 5σ point-source depths of stellar mass $\sim 10^{8.4} M_{\odot}$ at the redshift of CLJ1001 for a stellar population formed in a burst at redshift ~ 20 .

We compare the spatial distribution of molecular gas and stellar components for these member galaxies via their CO(3-2) intensity maps (moment-0) and JWST/NIRCam images. As shown in Fig. 2, some of these galaxies show more extended CO(3-2) distribution than their stellar components. While some of them are clearly mergers (4/20, M1 to M4) with peaks of gas emission between two galactic nuclei, the majority (9/20, disturbed galaxies: D1 to D9) are relatively isolated galaxies with visually classified asymmetric CO(3-2) structures. They generally feature gas elongation beyond the stellar component (D1 to D6) or gas disk offset from the galaxy center (D7 to D9). The extended gas structures of some disturbed galaxies (e.g., D1, D4 and D5 in lower panel

of Fig. 2) inherit the kinematics from the host rotation disk, indicating their origins from the host galaxies. The degree of morphological disturbance is further quantified by two parameters: the asymmetry of the CO(3-2) distribution relative to the center of the stellar component (A) and the radius of the CO(3-2) disks (r_{gas}). r_{gas} is derived as the mean distance of the pixels with half of the peak CO(3-2) flux from the emission peak, twice of which is the approximation of the full width at half maximum (FWHM) of the CO distribution. The two parameters describe the consistency between gas and stellar distribution, and the extension of the gas disks, respectively.

Left panel of Fig. 3 shows the distribution of the 16 non-merging CO(3-2)-detected members in the morphological parameter space. The visually classified disturbed galaxies exhibit systematically larger A and $r_{\text{gas}}/r_{\text{eff},\star}$ ($r_{\text{eff},\star}$ is the effective radius from ALMA PSF-convolved F444W image), while the classified “normal” galaxies (N1 to N7, CO moment-0 maps shown in figure S2) are more symmetric and compact. This verifies that the two populations have distinct molecular gas distribution. Given the typical positional accuracy better than $0.2''$ (8), those asymmetric structures cannot be explained by positional uncertainties solely, and external forces competing with the galaxy’s anchoring pressure should come into effect. Although some normal galaxies present disturbed gas disks in the outskirts (e.g. N2 and N5), they are much less prominent than the central high-surface density regions.

In general, two different kinds of environmental effects could account for the observed disturbed gas morphology: tidal stripping from galaxy-galaxy interactions (10, 11) and ram-pressure stripping (RPS) from galaxy-intracluster medium (ICM) interactions (12–15). The major difference between the two is that tidal stripping would also strip the stellar components. After examining the concentration and asymmetry of the stellar light distributions, we find that the disturbed galaxies in CLJ1001 have similar stellar morphologies as the normal cluster members and field galaxies at the same redshift except for D4 (figure S5). Therefore the gas disturbance in most of the disturbed galaxies is unlikely caused by tidal stripping, and RPS should be a more plausible reason. The detection of extended X-ray emission (2) and Sunyaev–Zeldovich effect (R. Gobat et al., in prep.) in CLJ1001 show that hot ICM is already present in at least some regions in this young cluster. Compared to local clusters, the ICM density in CLJ1001 should be over a dex higher with the higher critical density of the universe at $z = 2.51$, which would magnify the intensity of RPS events. Under the RPS scenario (16, 17), we calculate the truncation radius of the CLJ1001 galaxies, which is

around 1 – 2 effective radii of their gas distribution (8). Hence about 20%-50% of the gas could be easily disturbed and stripped from their host galaxies. CLJ1001 is not yet fully relaxed with signatures from velocity distributions of member galaxies, indicating that two prominent filaments are merging towards the cluster center (R. Gobat et al. in prep.). As a result, many galaxies could have larger velocities relative to the ICM during infalling compared to virialized systems, and the ICM itself could be quite clumpy, both of which may further enhance the RPS efficiency.

To gain further insights into the nature of the disturbed galaxies, we examine their distribution in the phase-space diagram in the right panel of Fig. 3. The locations of four disturbed galaxies (D5, D6, D7 and D9) in Fig. 3 are generally consistent with RPS galaxies seen in simulations or in local galaxy clusters (17, 18), in the inner cluster regions with a high density of ICM. They are likely accreted onto the cluster early and have been significantly stripped, further supported by their low gas fractions. The other disturbed galaxies are located in the outer cluster region with $R \geq 1 R_{200c}$, but with low relative velocity differences from the cluster center. This means that these galaxies fall nearly straight onto the cluster center with high radial velocities, which enhances the effect of RPS, as also shown in simulations (17, 19). Different from the RPS candidates in the center, those in the outer region are most likely going through their first infall, evidenced from their relatively high gas content. That is, the RPS may have just started for many of them as we observed, and has not removed a large portion of their cold gas.

Kinematical and star-formation properties of disturbed galaxies

To explore the effects of gas stripping on the properties of these cluster galaxies, we examine the stability in gas disks by deriving the resolved Toomre Q parameter (20) from CO(3-2) moment maps (8). We show the cumulative distribution function (CDF) of median Q parameter within stellar effective radius in Fig. 4. The disturbed galaxies have larger Q than the normal galaxies, except for N4. N4 hosts a radio active galactic nucleus (AGN) (2), whose gas could be disturbed by the AGN activity (21). Excluding this outlier, we plot the mean distribution of Q parameter along the distance to the galaxy center in Fig. 4. Again, the disturbed galaxies exhibit significantly larger Q within the inner $\sim 1.5 r_{\text{eff},\star}$ compared to the normal ones, suggesting more stable gas disks which contradict their star-forming states. Such high Q values are seen in simulated galaxies undergoing

perturbations (22), with gas compression in the turbulence and star-forming clumps formation later. Since Q is proportional to the velocity dispersion and anti-correlated with gas surface density, it is also the evidence for stripping scenario, which leads to low gas surface density and increased velocity dispersion in turbulence against the self-gravitational gas disk.

Molecular gas is the fuel for star formation, and in the right panel of Fig. 4, we find that the disturbed galaxies exhibit higher star formation efficiency ($SFE = SFR/M_{\text{gas}}$), about 0.35 dex higher than the normal galaxies. This appears to be mainly driven by their systematically lower gas surface densities, which are ~ 0.56 dex lower than that of normal SFGs in CLJ1001. Alternatively, enhanced star formation has also been observed in local RPS events (23, 24). These features are very supportive of the RPS origin for the disturbed galaxies, which globally exhibit low gas densities at given local gas surface densities due to RPS; in tandem, shock compression may increase the fraction of dense gas and hence further contribute to an enhanced SFE.

Our results have revealed various environmental effects at work in the forming cluster CLJ1001 at redshift $z = 2.51$. Especially, our observational evidence put forward the efficient RPS at the known highest redshift. The early-positioned ICM could enable the cluster environment to accelerate consuming and removing gas within the cluster galaxies, along with the tidal interactions and mergers. The environmental effects in CLJ1001-like structures in the early Universe which have relatively low halo masses and are actively assembling prove that the quenching of massive cluster galaxies not only happens in a mature cluster, but also happens at a earlier epoch.

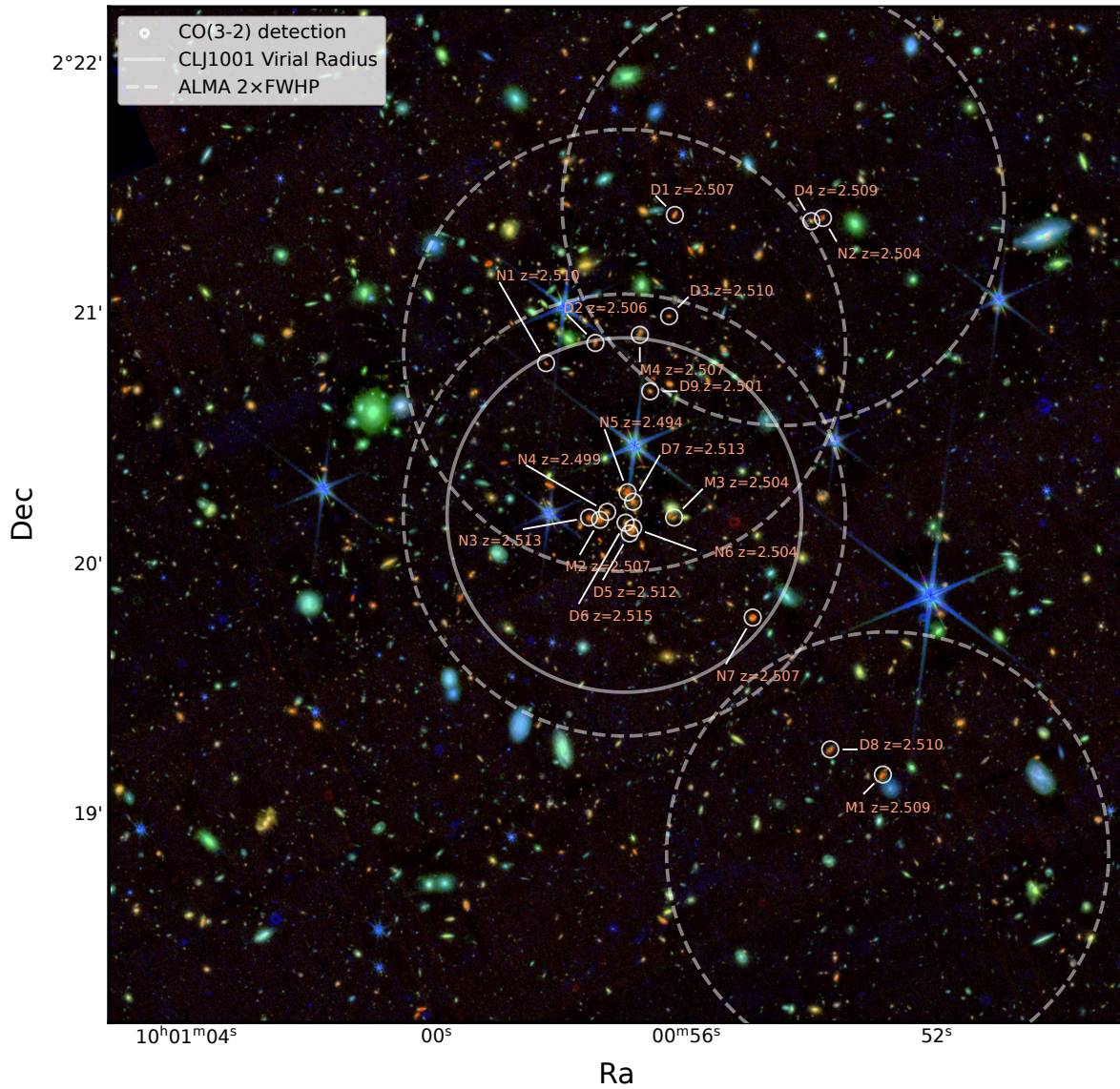


Figure 1: The sky image of CLJ1001. CO(3-2) detections are marked with IDs and redshifts in orange text on the JWST/NIRCam RGB image (R: F444W, G: F277W and B: F150W). The solid white circle shows the virial radius of CLJ1001 and the dashed white circles show the coverage of four ALMA pointings at 2× full-width at half power (FWHP).

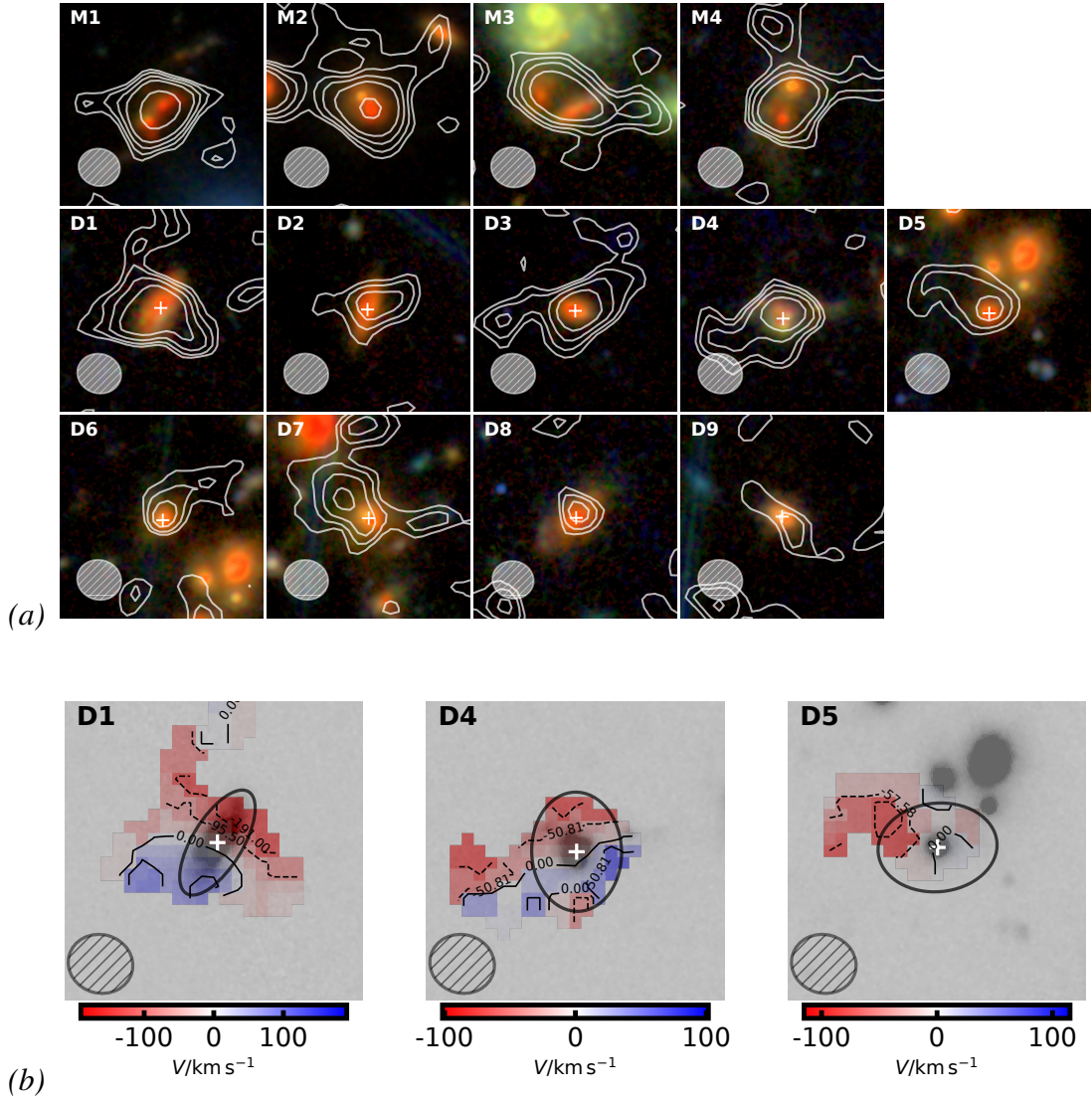


Figure 2: CO(3-2) moment-0 maps (white contours) on the false color JWST/NIRCam images for the mergers and disturbed galaxies and some example moment-1 maps on the F444W image. (a) The contour levels are $\sqrt{2}$, 2, $2\sqrt{2}$, 4, 8, 16 times the root mean square (RMS). The false color NIRCam images are made with F444W (R), F277W (G), and F150W (B) images. (b) The moment-1 maps are shown in the colormap with their colorbar below. The contours and inline numbers denote the velocity gradients and velocities (V). All panels are in size of $5'' \times 5''$. The white plus marks the center of the stellar component. The black ellipse at the center shows the galaxy morphology from PETROFIT. The ellipse in the lower left corner of each panel denotes the synthesized beam of CO(3-2) observations, and the ID of each galaxy is labeled in the upper left corner of each panel .

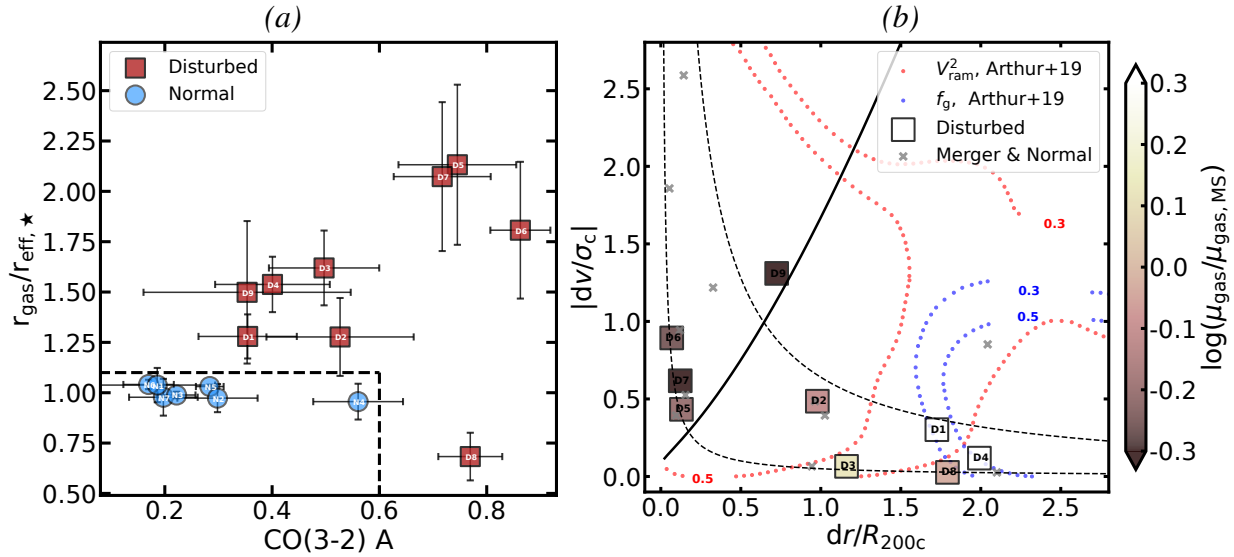


Figure 3: The morphological diagnostics and phase-space diagram of member galaxies in CLJ1001. (a) The plot between $r_{\text{gas}}/r_{\text{eff},\star}$ and A . The r_{gas} is the mean distance from the peak of gas disk to the positions with half flux of the peak value. The $r_{\text{eff},\star}$ is the galaxy effective radius in the ALMA resolution-convolved F444W image and the A is the asymmetry of gas distribution relative to the stellar center. The dashed line shows the demarcation for disturbed and normal galaxies. The error bars show 1σ standard deviation. (b) The phase-space plot for the disturbed galaxies in CLJ1001. X axis is the projected radius in sky (dr) normalized by the cluster virial radius (R_{200c}). Y axis is the velocity deviation from the cluster center divided by the cluster velocity dispersion (σ_c). The dv is calculated as $dv = |z_i - z_c|/(1 + z_c) \times c$, where c , z_i and z_c are light speed, redshifts of galaxies and CLJ1001, respectively. The two dashed lines denote $|dv/\sigma_c| \times (dr/R_{200c}) = 0.05$ and 0.64 , where σ_c and R_{200c} are from ref. (4). The blue and red dotted lines from ref. (19) show the gas fraction (f_g) and differential velocity (V_{ram}) between subhalos and the ICM, with the number showing the fraction of peak values. The black solid line shows the position of a main-sequence galaxy with $\log(M_{\star}/M_{\odot}) = 10.5$ and a truncation radius of $1.5 \times$ gas effective radius in the RPS (8). The data points are color-coded by the ratio of their gas fraction (μ_{gas}) to that of the field main-sequence galaxies ($\mu_{\text{gas,MS}}$) (25).

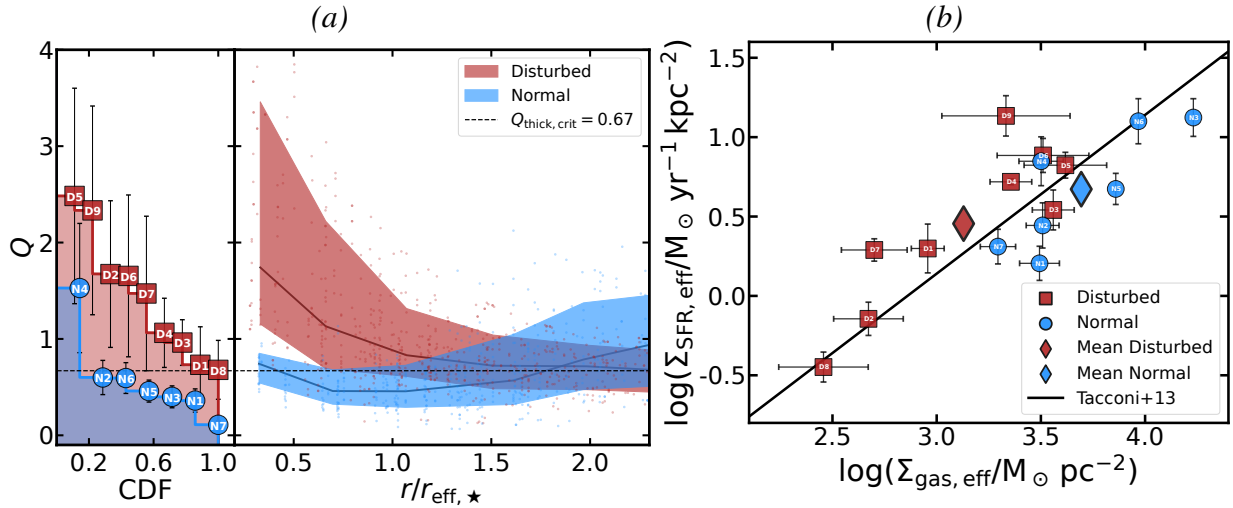


Figure 4: The Toomre Q parameter and star-formation relation for cluster member galaxies.

(a): Left panel shows the cumulative distribution function (CDF) of the median Toomre Q parameter within the stellar effective radius of cluster galaxies. The error bars show the 1σ standard derivation. The galaxies are shown at their appearance on the CDF. Right panel shows the spatially resolved Toomre Q parameter along the distance from galaxy centers. The red and blue small dots show the pixel values for disturbed and normal galaxies, with the solid line and its shaded region denote the median and standard deviation of the distribution. The horizontal dashed line is the critical value for a stable thick gas disk (26, 27), above which the gas disk should be stable. (b): The Kennicutt-Schmidt relation between star-formation rate surface density ($\Sigma_{\text{gas,eff}}$) and molecular gas surface density ($\Sigma_{\text{SFR,eff}}$) within the stellar effective radius. The solid line is from ref. (28) after converting the line luminosity to gas mass (8). The error bars show 1σ standard deviation.

References and Notes

1. T. B. Miller, *et al.*, A massive core for a cluster of galaxies at a redshift of 4.3. *Nature* **556** (7702), 469–472 (2018), doi:10.1038/s41586-018-0025-2.
2. T. Wang, *et al.*, Discovery of a Galaxy Cluster with a Violently Starbursting Core at $z = 2.506$. *ApJ* **828** (1), 56 (2016), doi:10.3847/0004-637X/828/1/56.
3. J. B. Champagne, *et al.*, Comprehensive Gas Characterization of a $z = 2.5$ Protocluster: A Cluster Core Caught in the Beginning of Virialization? *ApJ* **913** (2), 110 (2021), doi:10.3847/1538-4357/abf4e6.
4. T. Wang, *et al.*, Revealing the Environmental Dependence of Molecular Gas Content in a Distant X-Ray Cluster at $z = 2.51$. *ApJL* **867** (2), L29 (2018), doi:10.3847/2041-8213/aaeb2c.
5. C. Xu, *et al.*, Accelerated Structural Evolution of Galaxies in a Starbursting Cluster at $z = 2.51$. *ApJL* **951** (1), L21 (2023), doi:10.3847/2041-8213/acdb5a.
6. H. Sun, *et al.*, JWST's first glimpses of a $z > 2$ forming cluster reveals a top-heavy stellar mass function. *arXiv e-prints* arXiv:2403.05248 (2024), doi:10.48550/arXiv.2403.05248.
7. M. Y. Xiao, *et al.*, Starbursts with suppressed velocity dispersion revealed in a forming cluster at $z = 2.51$. *A&A* **664**, A63 (2022), doi:10.1051/0004-6361/202142843.
8. Materials and methods are available as supplementary material.
9. C. M. Casey, *et al.*, COSMOS-Web: An Overview of the JWST Cosmic Origins Survey. *ApJ* **954** (1), 31 (2023), doi:10.3847/1538-4357/acc2bc.
10. F. Combes, C. Dupraz, F. Casoli, L. Pagani, CO emission in NGC 4438 : a case for tidal stripping ? *A&A* **203**, L9–L12 (1988).
11. S. Alberts, A. Noble, From Clusters to Proto-Clusters: The Infrared Perspective on Environmental Galaxy Evolution. *Universe* **8** (11), 554 (2022), doi:10.3390/universe8110554.

12. A. G. Noble, *et al.*, Resolving CO (2-1) in $z \sim 1.6$ Gas-rich Cluster Galaxies with ALMA: Rotating Molecular Gas Disks with Possible Signatures of Gas Stripping. *ApJ* **870** (2), 56 (2019), doi:10.3847/1538-4357/aaf1c6.
13. A. Boselli, *et al.*, Evidence for ram-pressure stripping in a cluster of galaxies at $z = 0.7$. *A&A* **631**, A114 (2019), doi:10.1051/0004-6361/201936133.
14. A. Boselli, M. Fossati, M. Sun, Ram pressure stripping in high-density environments. *A&Ar* **30** (1), 3 (2022), doi:10.1007/s00159-022-00140-3.
15. W. J. Cramer, *et al.*, ALMA Evidence for Ram Pressure Compression and Stripping of Molecular Gas in the Virgo Cluster Galaxy NGC 4402. *ApJ* **901** (2), 95 (2020), doi:10.3847/1538-4357/abaf54.
16. J. E. Gunn, I. Gott, J. Richard, On the Infall of Matter Into Clusters of Galaxies and Some Effects on Their Evolution. *ApJ* **176**, 1 (1972), doi:10.1086/151605.
17. Y. L. Jaffé, *et al.*, BUDHIES II: a phase-space view of H I gas stripping and star formation quenching in cluster galaxies. *MNRAS* **448** (2), 1715–1728 (2015), doi:10.1093/mnras/stv100.
18. Y. L. Jaffé, *et al.*, GASP. IX. Jellyfish galaxies in phase-space: an orbital study of intense ram-pressure stripping in clusters. *MNRAS* **476** (4), 4753–4764 (2018), doi:10.1093/mnras/sty500.
19. J. Arthur, *et al.*, THETHREEHUNDRED Project: ram pressure and gas content of haloes and subhaloes in the phase-space plane. *MNRAS* **484** (3), 3968–3983 (2019), doi:10.1093/mnras/stz212.
20. A. Toomre, On the gravitational stability of a disk of stars. *ApJ* **139**, 1217–1238 (1964), doi:10.1086/147861.
21. S. Murthy, *et al.*, Cold gas removal from the centre of a galaxy by a low-luminosity jet. *Nature Astronomy* **6**, 488–495 (2022), doi:10.1038/s41550-021-01596-6.
22. S. Inoue, *et al.*, Non-linear violent disc instability with high Toomre’s Q in high-redshift clumpy disc galaxies. *MNRAS* **456** (2), 2052–2069 (2016), doi:10.1093/mnras/stv2793.

23. B. Vulcani, *et al.*, Enhanced Star Formation in Both Disks and Ram-pressure-stripped Tails of GASP Jellyfish Galaxies. *ApJL* **866** (2), L25 (2018), doi:10.3847/2041-8213/aae68b.
24. J. Zhu, S. Tonnesen, G. L. Bryan, When and How Ram Pressure Stripping in Low-mass Satellite Galaxies Enhances Star Formation. *ApJ* **960** (1), 54 (2024), doi:10.3847/1538-4357/acfe6f.
25. L. J. Tacconi, *et al.*, PHIBSS: Unified Scaling Relations of Gas Depletion Time and Molecular Gas Fractions. *ApJ* **853** (2), 179 (2018), doi:10.3847/1538-4357/aaa4b4.
26. R. Genzel, *et al.*, The Sins Survey of $z \sim 2$ Galaxy Kinematics: Properties of the Giant Star-forming Clumps. *ApJ* **733** (2), 101 (2011), doi:10.1088/0004-637X/733/2/101.
27. M. Cacciato, A. Dekel, S. Genel, Evolution of violent gravitational disc instability in galaxies: late stabilization by transition from gas to stellar dominance. *MNRAS* **421** (1), 818–831 (2012), doi:10.1111/j.1365-2966.2011.20359.x.
28. L. J. Tacconi, *et al.*, Phibss: Molecular Gas Content and Scaling Relations in $z \sim 1-3$ Massive, Main-sequence Star-forming Galaxies. *ApJ* **768** (1), 74 (2013), doi:10.1088/0004-637X/768/1/74.
29. ALMA Science Archive, ALMA Science Archive, <https://almascience.eso.org/aq>.
30. MAST, MAST, <https://archive.stsci.edu/doi/resolve/resolve.html?doi=10.17909/1r9y-dv80>.
31. C. R. Harris, *et al.*, Array programming with NumPy. *Nature* **585** (7825), 357–362 (2020), doi:10.1038/s41586-020-2649-2.
32. Astropy Collaboration, *et al.*, Astropy: A community Python package for astronomy. *A&A* **558**, A33 (2013), doi:10.1051/0004-6361/201322068.
33. J. D. Hunter, Matplotlib: A 2D Graphics Environment. *Computing in Science and Engineering* **9** (3), 90–95 (2007), doi:10.1109/MCSE.2007.55.
34. R. Geda, *et al.*, PetroFit: A Python Package for Computing Petrosian Radii and Fitting Galaxy Light Profiles. *AJ* **163** (5), 202 (2022), doi:10.3847/1538-3881/ac5908.

35. J. P. McMullin, B. Waters, D. Schiebel, W. Young, K. Golap, CASA Architecture and Applications, in *Astronomical Data Analysis Software and Systems XVI*, R. A. Shaw, F. Hill, D. J. Bell, Eds., vol. 376 of *Astronomical Society of the Pacific Conference Series* (2007), p. 127.
36. X. Ding, S. Birrer, T. Treu, J. D. Silverman, Galaxy shapes of Light (GaLight): a 2D modeling of galaxy images. *arXiv e-prints* arXiv:2111.08721 (2021), doi:10.48550/arXiv.2111.08721.
37. A. C. Carnall, R. J. McLure, J. S. Dunlop, R. Davé, Inferring the star formation histories of massive quiescent galaxies with BAGPIPES: evidence for multiple quenching mechanisms. *MNRAS* **480** (4), 4379–4401 (2018), doi:10.1093/mnras/sty2169.
38. L. Bradley, *et al.*, astropy/photutils: 1.0.0 (2020), doi:10.5281/zenodo.4044744.
39. P. Virtanen, *et al.*, SciPy 1.0: fundamental algorithms for scientific computing in Python. *Nature Methods* **17**, 261–272 (2020), doi:10.1038/s41592-019-0686-2.
40. S. van der Walt, *et al.*, scikit-image: Image processing in Python. *PeerJ* **2**, e453 (2014), doi:10.7717/peerj.453.
41. P. Kroupa, C. M. Boily, On the mass function of star clusters. *MNRAS* **336** (4), 1188–1194 (2002), doi:10.1046/j.1365-8711.2002.05848.x.
42. H. J. McCracken, *et al.*, UltraVISTA: a new ultra-deep near-infrared survey in COSMOS. *A&A* **544**, A156 (2012), doi:10.1051/0004-6361/201219507.
43. D. D. Lenz, T. R. Ayres, Errors Associated with Fitting Gaussian Profiles to Noisy Emission-Line Spectra. *PASP* **104**, 1104 (1992), doi:10.1086/133096.
44. L. D. Anderson, *et al.*, Methods for Averaging Spectral Line Data. *PASP* **135** (1053), 114504 (2023), doi:10.1088/1538-3873/ad0444.
45. M. Cappellari, Voronoi binning: Optimal adaptive tessellations of multi-dimensional data. *arXiv e-prints* arXiv:0912.1303 (2009), doi:10.48550/arXiv.0912.1303.
46. C. J. Conselice, The Relationship between Stellar Light Distributions of Galaxies and Their Formation Histories. *Astrophysical Journal Supplement Series* **147** (1), 1–28 (2003), doi:10.1086/375001.

47. D. Nurgaliev, *et al.*, A Robust Quantification of Galaxy Cluster Morphology Using Asymmetry and Central Concentration. *ApJ* **779** (2), 112 (2013), doi:10.1088/0004-637X/779/2/112.
48. P. M. Solomon, P. A. Vanden Bout, Molecular Gas at High Redshift. *ARA&A* **43** (1), 677–725 (2005), doi:10.1146/annurev.astro.43.051804.102221.
49. D. Calzetti, *et al.*, The Dust Content and Opacity of Actively Star-forming Galaxies. *ApJ* **533** (2), 682–695 (2000), doi:10.1086/308692.
50. G. Bruzual, S. Charlot, Stellar population synthesis at the resolution of 2003. *MNRAS* **344** (4), 1000–1028 (2003), doi:10.1046/j.1365-8711.2003.06897.x.
51. N. Byler, J. J. Dalcanton, C. Conroy, B. D. Johnson, Nebular Continuum and Line Emission in Stellar Population Synthesis Models. *ApJ* **840** (1), 44 (2017), doi:10.3847/1538-4357/aa6c66.
52. A. Patej, A. Loeb, A Simple Physical Model for the Gas Distribution in Galaxy Clusters. *ApJL* **798** (1), L20 (2015), doi:10.1088/2041-8205/798/1/L20.
53. A. Morandi, M. Sun, W. Forman, C. Jones, The galaxy cluster outskirts probed by Chandra. *MNRAS* **450** (3), 2261–2278 (2015), doi:10.1093/mnras/stv660.
54. P. Jáchym, *et al.*, Molecular Gas Dominated 50 kpc Ram Pressure Stripped Tail of the Coma Galaxy D100. *ApJ* **839** (2), 114 (2017), doi:10.3847/1538-4357/aa6af5.
55. A. van der Wel, *et al.*, 3D-HST+CANDELS: The Evolution of the Galaxy Size-Mass Distribution since $z = 3$. *ApJ* **788** (1), 28 (2014), doi:10.1088/0004-637X/788/1/28.
56. K. Tadaki, *et al.*, The gravitationally unstable gas disk of a starburst galaxy 12 billion years ago. *Nature* **560** (7720), 613–616 (2018), doi:10.1038/s41586-018-0443-1.
57. J. Binney, S. Tremaine, *Galactic Dynamics: Second Edition* (2008).
58. L. Cortese, *et al.*, The SAMI Galaxy Survey: the link between angular momentum and optical morphology. *MNRAS* **463** (1), 170–184 (2016), doi:10.1093/mnras/stw1891.
59. ALMA Technical handbook, ALMA Technical handbook, <https://almascience.nrao.edu/proposing/technical-handbook>.

60. J. S. Speagle, C. L. Steinhardt, P. L. Capak, J. D. Silverman, A Highly Consistent Framework for the Evolution of the Star-Forming “Main Sequence” from $z \sim 0-6$. *ApJs* **214** (2), 15 (2014), doi:10.1088/0067-0049/214/2/15.

Acknowledgments

This work was supported by National Natural Science Foundation of China (Project No. 12173017 and Key Project No. 12141301), National Key R&D Program of China (2023YFA1605600), and the China Manned Space Project (No. CMS-CSST-2021-A07).

Author contributions: K. X. reduced the ALMA data, contributed to the main results, and authored the text under the supervision of T.W.. T. W. initiated the study, interpreted the main results, and improved the text. H. S. reduced the JWST data and aided with the photometric measurement for SED fitting. L. C. helped with the galaxy morphology measurements. E. D., D. E., R. G., A. Z., D. L., M. X., R. C., T. K., K. K., T. Y., Z. Z., L. Z., and F. V. contributed to the overall interpretation of the results and the analysis.

Competing interests: There are no competing interests to declare.

Data and materials availability: The ALMA data are available via ALMA Archive (29). The JWST/NIRCam images are available from the MAST (6,30). All codes used in the paper are publicly available, including NUMPY (31), ASTROPY (32), MATPLOTLIB (33), PETROFIT (34), CASA (35), GALIGHT (36), BAGPIPES (37), PHOTUTILS (38), SciPY (39), SCIKIT-IMAGE (40).

Supplementary materials

Materials and Methods

Figs. S1 to S8

Tables S1

References (29-60)

Supplementary Materials for
Ram-pressure stripping caught in action in a forming galaxy
cluster 3 billion years after the Big Bang

Ke Xu^{1,2}, Tao Wang^{1,2*}, Emanuele Daddi³, David Elbaz³, Hanwen Sun^{1,2}, Longyue Chen^{1,2},
Raphael Gobat⁴, Anita Zanella⁵,
Daizhong Liu⁶, Mengyuan Xiao⁷, Renyue Cen⁸, Tadayuki Kodama⁹,
Kotaro Kohno^{10,11}, Tiancheng Yang^{1,2}, Zhi-Yu Zhang^{1,2},
Luwenjia Zhou^{1,2}, Francesco Valentino^{12,13,14}

*Corresponding author. Email: taowang@nju.edu.cn

This PDF file includes:

Materials and Methods

Figures S1 to S8

Tables S1

Materials and Methods

Throughout this work, we adopt the standard Λ CDM cosmology with $H_0 = 70 \text{ km s}^{-1} \text{ Mpc}^{-1}$, $\Omega_M = 0.3$ and $\Omega_\Lambda = 0.7$, and the stellar initial mass function from ref. (41).

CLJ1001 locates in the COSMOS field with multi-band observations, including VISTA/K band (42), JWST/NIRCam (9), Subaru/MORICS CO narrow band (rest-frame $\sim 2.3 \mu\text{m}$) observation (PI: T. Kodama), and JWST COSMOS-Web survey (9). More details are summarized in ref. (6).

ALMA data, source detection and classification

We carried out observations of the CO(3-2) transitions (rest-frame frequency 345.796 GHz) for galaxies in CLJ1001 at $z = 2.51$ with ALMA band 3. These observations were taken between 2016 November 21 and 2018 January 13 (Project ID: 2016.1.01155.S and 2017.1.01099; PI: Tao Wang). Project: 2016.1.01155.S in ALMA Cycle 4 consisted of two different array configurations towards the pointing at the cluster center, the more compact C40-4 and the more extended C40-7 with integration time ~ 1.1 h and 2.2 h, respectively. Project: 2017.1.01099 in ALMA Cycle 5 targets the two upper and one bottom areas out to $\sim 3 \times R_{200c}$, observing in array C43-6 with integration time ~ 4.2 h in each pointing. The full-width at half power (FWHP) of the ALMA primary beam of each pointing is $\sim 53''$.

We performed the data calibration using pipeline in the Common Astronomy Software Application package (35) (CASA; in version 4.7.2, 4.7.0 and 5.1.1 for individual observations). And we used CASA 6.2.1.7 for data products and visualization after the calibration. We combined the visibility data and used `TCLEAN` with $0.2''$ cell size, a `uvtaper` of $0.6''$, a channel width of 16 MHz, Briggs weighting of `robust=2` and 2.5σ threshold. To obtain the CO(3-2) line data cube, we performed `IMCONTSUB` task in CASA with linear continuum subtraction. The output data cube has an averaged synthesized beam size of $1.09'' \times 0.98''$ (and $1.02'' \times 0.93''$ for the lower single pointing, ~ 8 kpc in the physical scale) and a RMS level of $\sim 90 \mu\text{Jy beam}^{-1}$ per channel at the phase center.

We also clean a high-resolution data cube using the weighted visibility data (for central pointing, we assigned the weights of the compact array to the extended array as 1:4 to match the average resolution in the other pointings) with Briggs weighting of `robust=1.5` and a `uvtaper` of $0.3''$ for

further data presentation. The resolution of the returned high-resolution data cube is $0.66'' \times 0.58''$.

Ref (6) selected a list of cluster members based on the photometric redshifts and $H\alpha$ emission. We first extracted the spectrum from CO(3-2) data cube centered at these $H\alpha$ emitters, which returns 19 detections with $\text{SNR} > 4$ (except for weak detection of D8 and D9 with $\text{SNR} \sim 3$), including the four galaxies presented in ref. (7) and 13 of the CO(1-0)-detected galaxies presented in ref. (2, 4). The velocity range is determined from the velocity-integrated fluxes with maximum signal-to-noise ratio (SNR). We also detected sources directly from the CO(3-2) data cube. For every pixel in the data cube, we subtracted the spectrum within $2 \times$ synthesized beam and collapsed the data cube in the velocity range then flagged it whether it is the local brightest peak. If true, we tried to find the optical counterpart with photometric redshift ~ 2.51 . We required the source with $\text{SNR} \geq 4$ within a synthesized beam. The SNR is calculated as (43, 44):

$$\text{SNR} = 0.7 \left(\frac{\Delta V}{\Delta v} \right)^{0.5} \frac{f_{\text{peak}}}{\sigma_{\text{RMS}}}, \quad (\text{S1})$$

where Δv , f_{peak} and σ_{RMS} are the spectrum resolution, peak flux and RMS. The RMS is estimated in the negative channels. The 0.7 is corresponding to a Gaussian line profile. ΔV is the full width at half maximum (FWHM) of the emission line by fitting the Gaussian to the spectrum. In this way, we got one new detection (galaxy N1) besides the previous 19 detections. And we list the information of these sources in extended Table S1.

With a large sample of spectroscopic members including extra four $H\alpha$ emitters from ref. (2)), we re-derive the central redshift of the cluster by fitting a Gaussian function to the redshift distribution (using `CURVEFIT` in `SCIPLY` (39)), yielding $z_c = 2.510 \pm 0.002$ (Figure S1). This is slightly different from the value reported in ref. (2) ($z_c = 2.506$), which is likely due to the smaller sample of spectroscopic members in ref. (2) and the fact that the early-confirmed members include mostly galaxies in the cluster core. The result is shown in Figure S1.

We used task `IMMOMENTS` in `CASA` to create the CO(3-2) moment-0 (flux), moment-1 (line-of-sight velocity) and moment-2 (velocity dispersion) images. We correct the effect of beam smearing in moment-2 maps by deducting the standard deviation of moment-1 maps within a synthesized beam at each pixels. Because low-SNR pixel in moment-0 could result in unreliable velocity subtraction, we utilized package `VORBIN` (45) to make bins of $\text{SNR} > 5$ based on the moment-0 maps and then binned the moment-1, moment-2 maps in the same manners. We show the moment-

1 images in Figure S7.

We fit the sersic profile using `PETROFIT` (34) for cluster galaxies in F444W images, which returns the effective radius ($r_{\text{eff},\star}$), Sérsic index, the position angle and the center position of the stellar component.

Because the ALMA observation has larger PSF than the JWST observation, we should only use the effective radius from F444W image after convolution with the ALMA synthesized beam when comparing with the ALMA data. We first convolved the F444W image with the ALMA synthesized beam and then fitted it with Gaussian by `PETROFIT` at the center from the fitting in the un-convolved F444W image. We adopted the half-light radius of the output Gaussian model as the convolved effective radius (which is also the FWHM for a 2D Gaussian). We note that we mean the convolved effective radius when comparing between the ALMA and JWST observation.

In Figure S5, we also show the distribution of the stellar concentration and asymmetry of cluster members and some field galaxies in the COSMOS field (L. Chen et al., in prep.) at $2 < z < 3$ computed from `GALIGHT` (36).

Because the cluster galaxies undergoing environmental effects could have asymmetric or one-sided gas distribution, to classify the galaxy based on their gas morphology, we define an approximate radius r_{gas} , for the gas disks. To calculate r_{gas} , in CO(3-2) moment-0 maps for each galaxy, we only reserved pixel values with $\text{SNR} \geq \sqrt{2} \sigma$, where σ is the RMS of the negative values in the map. We used function `REMOVING_SMALL_OBJECTS` in Python package `Scikit-image` (40) to reserve the largest connected domain associated to the host galaxies, in avoidance of the noises. The peak of CO(3-2) emission is determined by Python package `PHOTUTILS` (38). Then the r_{gas} was derived from the mean distance of pixels with the half flux of the maximum to the peak position, and we took the standard deviation as errors.

Next, we derived the non-parametric morphology parameter, asymmetry (A), following refs. (46, 47):

$$A = \frac{\sum |I_0 - I_{180}|}{2 \sum |I_0|}, \quad (\text{S2})$$

where I_0 and I_{180} are the original image and image rotated 180 degrees around the center position of the stellar component. To estimate the errors of r_{gas} and A , we performed 1000 random runs. In each run, we calculated the two parameters for a noise-added Gaussian model with the same CO(3-2) peak amplitudes and stellar effective radii as the cluster galaxies, and adopted the standard

derivation as the errors.

We plot the galaxies in the $r_{\text{gas}}/r_{\text{ff},\star} - A$ plane in the left panel of Fig. 3. A clear existence of a group with larger A and larger r_{gas} over the stellar component indicates the asymmetric elongated gas structures. Thus we adopted the demarcation line in Fig. 3 to divide disturbed and normal galaxies. We also tried to fit a Gaussian to the CO(3-2) distribution, and the result is consistent to what we have here. But because of the asymmetric gas morphology, a single Gaussian could not fully describe their distribution. While the merger and disturbed galaxies are shown in Fig. 2, the normal galaxies are shown in Figure S3.

For better presentation, we also contour the moment-0 maps integrated in the same velocity range from the high-resolution data cube on the JWST RGB image in Figure S4. The disturbed galaxies could also be identified with the off-center/elongated features from the high-resolution image.

To further show the significance of the emission outside the main part of galaxies, we compared these signals to the background noise level. First, in the moment-0 maps, we fit the Gaussian function to the distribution of noise within a synthesized beam exclusively with negative values to avoid including any unclassified emission. Then the fluxes from apertures of the same shape as the synthesized beam around the galaxies are derived and compared to the noise standard derivation. We show the significance of these extended emission for D1-D5 in Figure S6.

We note that the above significance test would underestimate the significance of our disturbed galaxies, because the continuity in the velocity, the irregular and extended shapes in spatial distribution have not been well accounted for.

Derive physical properties of the cluster galaxies

To derive molecular gas masses (M_{mol}) and the gas fractions (μ_{gas}), in CO(3-2) moment-0 image, we first obtained the resolved velocity integrated flux ($S_{\text{CO}\Delta v}$). By using equation 3 in ref. (48) to convert the $S_{\text{CO}\Delta v}$ into CO(3-2) line luminosity ($L'_{\text{CO}3-2}$), the line ratio between CO(3-2) and CO(1-0), $R_{31} = 0.7$ (mean value in ref. (7)), the CO to H_2 conversion factor $\alpha_{\text{CO}} = 4.10$ (mean value in ref. (4)) and a factor of 1.36 for Helium contribution, we derived the resolved M_{mol} for these galaxies. The μ_{gas} is determined by the μ_{gas} within the ALMA synthesized beam-convolved stellar effective radius (where the stellar mass is approximated to be the half of the total).

To derive the star-formation rate (SFR) and stellar masses (M_{\star}), we performed the SED fitting with BAGPIPES (37). We applied the delayed star-formation history, Calzetti extinction law (49) stellar population synthesis model from 2016 version of BC03 (50) and nebular emission (51), with more details summarized in ref. (6). We show their locations relative to the star-formation main sequence in Figure S8. The SFR in the effective radius is simply assumed to be the half of the total SFR.

To derive the truncation radius (R_{trunc}), we used the classical criterion for ram-pressure stripping (16):

$$\rho_{\text{ICM}} V^2 \geq 2\pi G \Sigma_{\star} \Sigma_{\text{gas}}. \quad (\text{S3})$$

We adopted the ICM models from refs. (14, 52, 53), the stacking results of 320 clusters. We adopted cluster mass $\log(M_{200c}/M_{\odot}) = 13.78$, $R_{200c} = 340$ kpc (2, 4), the baryon fraction of 0.158 and the gas fraction of 0.9. We assumed the clustercentric distance to be $\sqrt{3/2} \times$ sky projected distance. We computed the stellar and gas surface density as (17):

$$\begin{aligned} \Sigma_{\star} &= \Sigma_{0,\star} e^{-r/(r_{\text{eff},\star}/1.678)}, & \Sigma_{0,\star} &= \frac{M_{\star}}{2\pi (r_{\text{eff},\star}/1.678)^2}, \\ \Sigma_{\text{gas}} &= \Sigma_{0,\text{gas}} e^{-r/(r_{\text{eff,gas}}/1.678)}, & \Sigma_{0,\text{gas}} &= \frac{M_{\text{gas}}}{2\pi (r_{\text{eff,gas}}/1.678)^2}, \end{aligned} \quad (\text{S4})$$

where the value 1.678 is the conversion factor between the scale length and the effective radius of an exponential disk.

We used the relation in ref. (25) to calculate M_{mol} in main sequence at galaxy stellar masses and the effective radius of gas disks was assumed to be $r_{\text{eff,gas}} = 2 \times r_{\text{eff},\star}$. Taking the infalling velocity of 1500 km/s (54), comparable to the free-fall velocity from infinity to $1 R_{200c}$, we computed at which radius (R_{trunc}), Eq. S3 would reach the balance. Generally, the cluster galaxies have $R_{\text{trunc}} \sim 1 - 2 r_{\text{eff,gas}}$, which means 20%-50% of the gas would be influenced by the cluster environment. The ram-pressure stripping criterion (Eq. S3) is applicable to the case where the velocity vector of the galaxy is perpendicular to its gas disk with the ram-pressure stripping being maximized. The larger the angle is between the velocity vector and the disk normal, the more difficult is for the ram-pressure effect to occur. Thus, ram-pressure stripping is a threshold phenomenon. As such, it is likely that the most visible ram-pressure effects occur in the maximum scenario. An importance consequence in this scenario is that the dislodged gas still in the vicinity of its former host galaxy is expected to display a rotational signature conformal to the host galaxy. Upon

a closer examination, we find galaxies D1, D4 and D5 show such signatures. We defer detailed quantification of this signature to a future study, with the aid of numerical simulations.

To derive the solid line in the right panel of Fig. 3, we further use the mass-size relation from ref. (55).

To derive the Kennicutt-Schmidt law in Fig. 3, we performed aperture photometry with PHOTUTILS within stellar effective radius (convolved with the synthesized beam) on the CO(3-2) moment-0 maps. Because the resolved SFR is unavailable given the limited ground-based photometry, we simply assume half of the total SFR in the effective radius.

To convert the $\text{SFR} - L_{\text{CO}3-2}$ relation in ref. (28) to $\Sigma_{\text{SFR}} - \Sigma_{\text{mol}}$ relation, we adopted the same conversion factors as our CO detected galaxies.

To derive the spatially resolved Q parameter in each pixel, we calculated as ref. (56):

$$Q = \kappa \sigma_{\text{gas}} / (\pi G \Sigma_{\text{mol}}), \quad (\text{S5})$$

where σ_{gas} is velocity dispersion from the CO(3-2) moment-2 maps corrected for beam smearing, Σ_{mol} is gas surface density from the CO(3-2) moment-0 maps and κ is the epicyclic frequency. We followed ref. (56, 57) with $\kappa = 1.4V_{\text{max}}/r$ at distance r from the galaxy center. And the V_{max} was taken as the maximum of $V_{90} - V_{\text{cen}}$ and $V_{\text{cen}} - V_{10}$, where V_{90} , V_{10} and V_{cen} are 90th and 10th percentiles in the CO(3-2) moment-1 maps and the velocity at the stellar center after inclination corrections. The inclination is determined from the galaxy axis ratio (b/a) by assuming the typical intrinsic axis ratio of edge-on galaxies $q_0 = 0.4$ (58):

$$\cos i = \sqrt{\frac{(b/a)^2 - q_0^2}{1 - q_0^2}} \quad (\text{S6})$$

The position accuracy of ALMA observation is calculated according to ALMA technical handbook (59):

$$\text{pos}_{\text{acc}} = \text{beam}_{\text{FWHM}} / (\text{SNR} \times 0.9), \quad (\text{S7})$$

where $\text{beam}_{\text{FWHM}}$ is the FWHM of the synthesized beam and SNR is the signal-to-noise ratio of the image target peak. With typical SNR greater than 6, the position accuracy is greater than $\sim 0.2''$. For some galaxies hardly resolved in low-resolution data cube, the SNR is relatively low for including the noises within a resolution. For these galaxies, we examine their SNR (larger than 4) in the high-resolution data cube, and they still have the pointing accuracy better than $\sim 0.2''$.

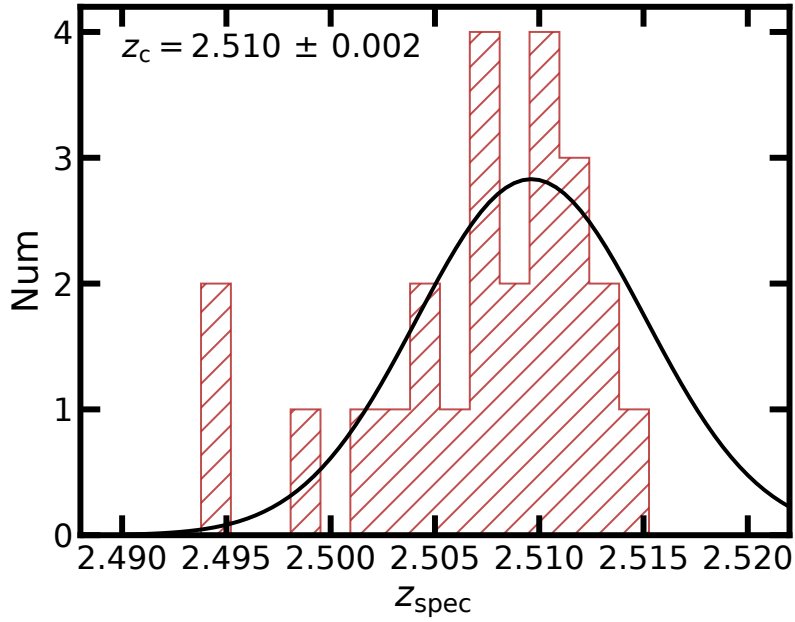


Figure S1: The redshift distribution of spectroscopically confirmed cluster members in CLJ1001. The solid line denote the best-fitted Gaussian distribution.

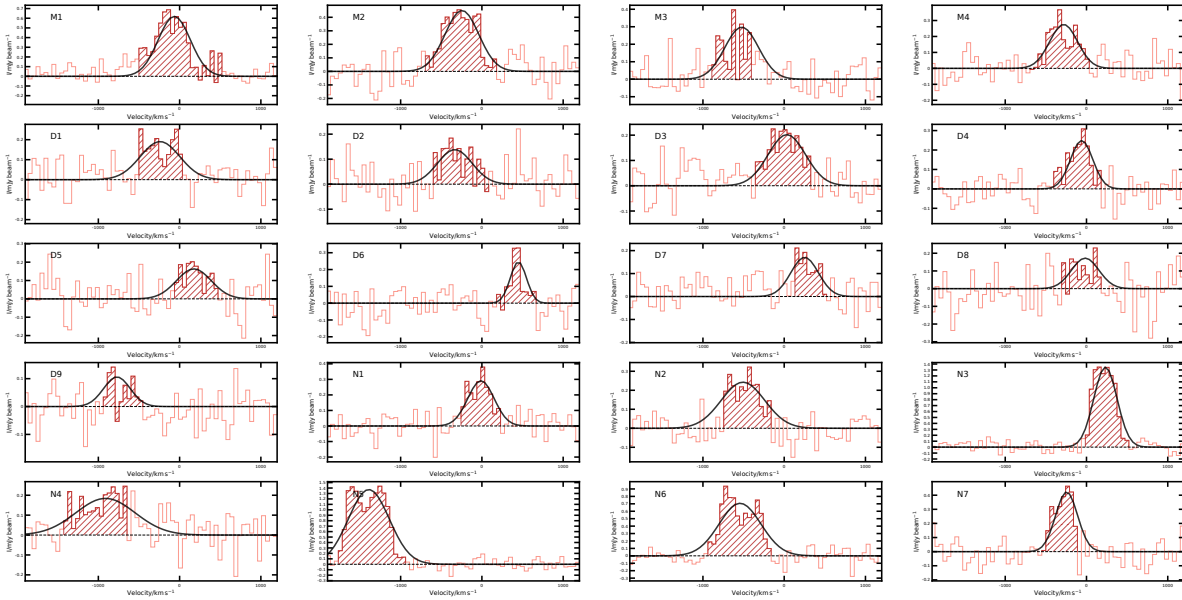


Figure S2: The CO(3-2) spectral line of detected cluster galaxies. Each panel shows the CO(3-2) line emission within $1 \times \text{FWHM}$ of the synthesized beam centered at the galaxy. The shaded region is the velocity range. The black solid line is the Gaussian fit to the emission line.

Table S1: Physical Properties of the CO(3-2)-detected Cluster Members in CLJ1001. *a*: the redshift of the CO(3-2) spectral lines from the Gaussian fitting (Figure S1). The typical error is $\lesssim 0.001$. *b*: the aperture photometry on CO(3-2) moment-0 map within convolved stellar effective radius. *c*: the global star-formation rate from SED fitting. *d*: the unconvolved effective radius from Sérsic model in JWST/F444W image.

Galaxy	Ra	Dec	$z_{\text{CO}3-2}^a$	$\log M_{\star}$ (M_{\odot})	$\log L_{\text{CO}3-2,\text{eff}}^b$ ($\text{K km s}^{-1} \text{pc}^2$)	$\log \text{SFR}^c$ ($M_{\odot} \text{yr}^{-1}$)	r_{gas} ($''$)	$r_{\text{eff},\star}^d$ ($''$)
M1	150.22026	2.31932	2.509
M2	150.23913	2.33633	2.507
M3	150.23421	2.33648	2.504
M4	150.23647	2.34871	2.507
D1	150.23412	2.35662	2.507	10.40±0.17	9.64±0.08	2.19±0.15	0.89±0.08	0.44
D2	150.23942	2.34809	2.506	10.55±0.06	9.32±0.17	1.70±0.10	0.86±0.14	0.42
D3	150.23452	2.34986	2.510	10.47±0.06	9.50±0.10	1.68±0.13	0.98±0.12	0.18
D4	150.22502	2.35619	2.509	9.98±0.04	9.48±0.10	2.04±0.02	1.07±0.09	0.23
D5	150.23715	2.33538	2.512	10.54±0.05	9.21±0.20	1.62±0.08	1.20±0.22	0.12
D6	150.23741	2.33609	2.515	10.56±0.05	9.17±0.22	1.75±0.11	1.15±0.23	0.13
D7	150.23691	2.33750	2.513	10.89±0.05	9.19±0.16	2.99±0.07	1.40±0.28	0.35
D8	150.22377	2.32100	2.510	10.64±0.10	9.45±0.21	1.75±0.09	0.49±0.09	0.62
D9	150.23578	2.34486	2.501	10.62±0.08	8.86±0.31	1.86±0.13	0.91±0.20	0.12
N1	150.24272	2.34674	2.510	10.30±0.06	9.55±0.10	1.47±0.11	0.64±0.05	0.21
N2	150.22426	2.35642	2.504	10.53±0.12	9.59±0.08	1.73±0.14	0.60±0.04	0.22
N3	150.23986	2.33645	2.513	11.04±0.07	10.12±0.02	2.21±0.12	0.61±0.01	0.17
N4	150.23864	2.33682	2.499	11.03±0.04	9.51±0.11	2.06±0.15	0.62±0.06	0.20
N5	150.23728	2.33813	2.494	11.30±0.05	10.31±0.01	2.33±0.10	0.62±0.01	0.33
N6	150.23691	2.33577	2.504	11.02±0.08	10.03±0.03	2.37±0.14	0.62±0.01	0.21
N7	150.22891	2.32984	2.507	10.99±0.06	10.15±0.08	2.37±0.11	0.69±0.07	0.54

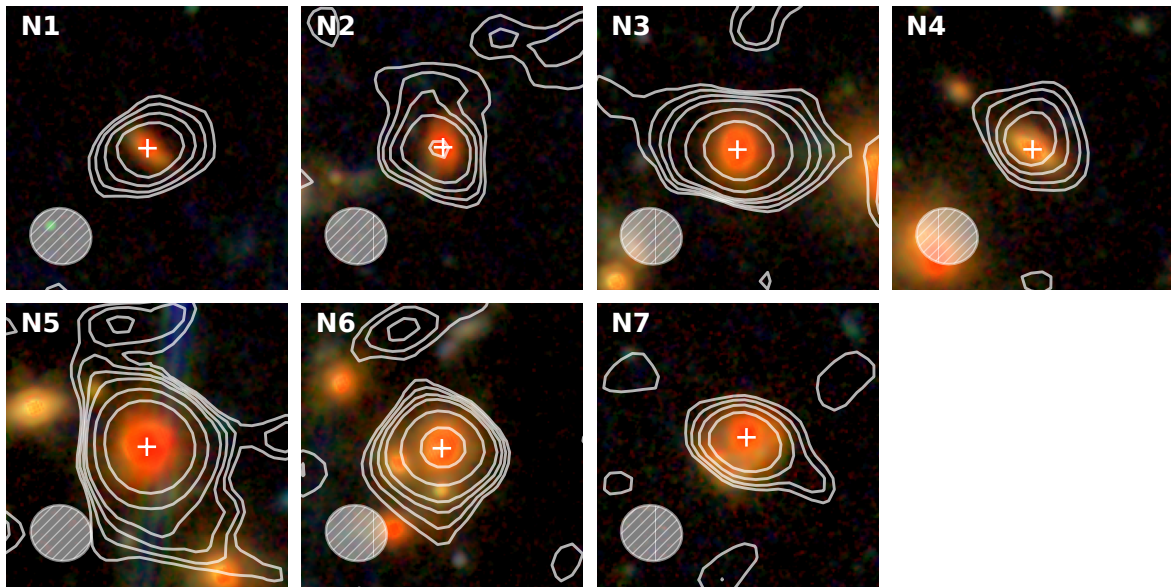


Figure S3: The distribution of CO(3-2) line emission for the normal cluster galaxies . The same as Fig. 2, but we show the normal galaxies here.

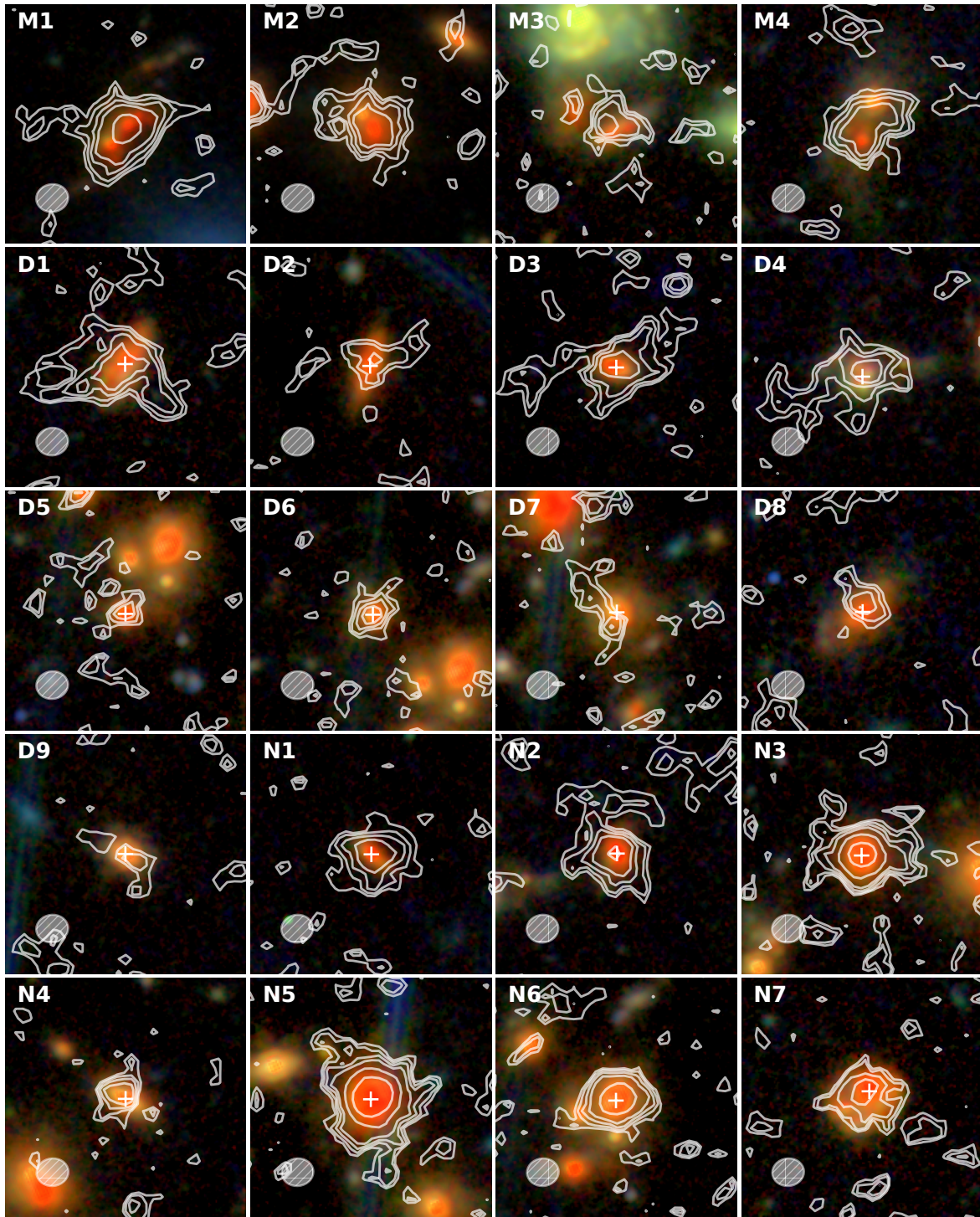


Figure S4: The high-resolution CO(3-2) distribution for detected cluster members. The same as Fig. 2, but each panel show the CO(3-2) line emission contoured on the JWST RGB image from the high-resolution data cube.

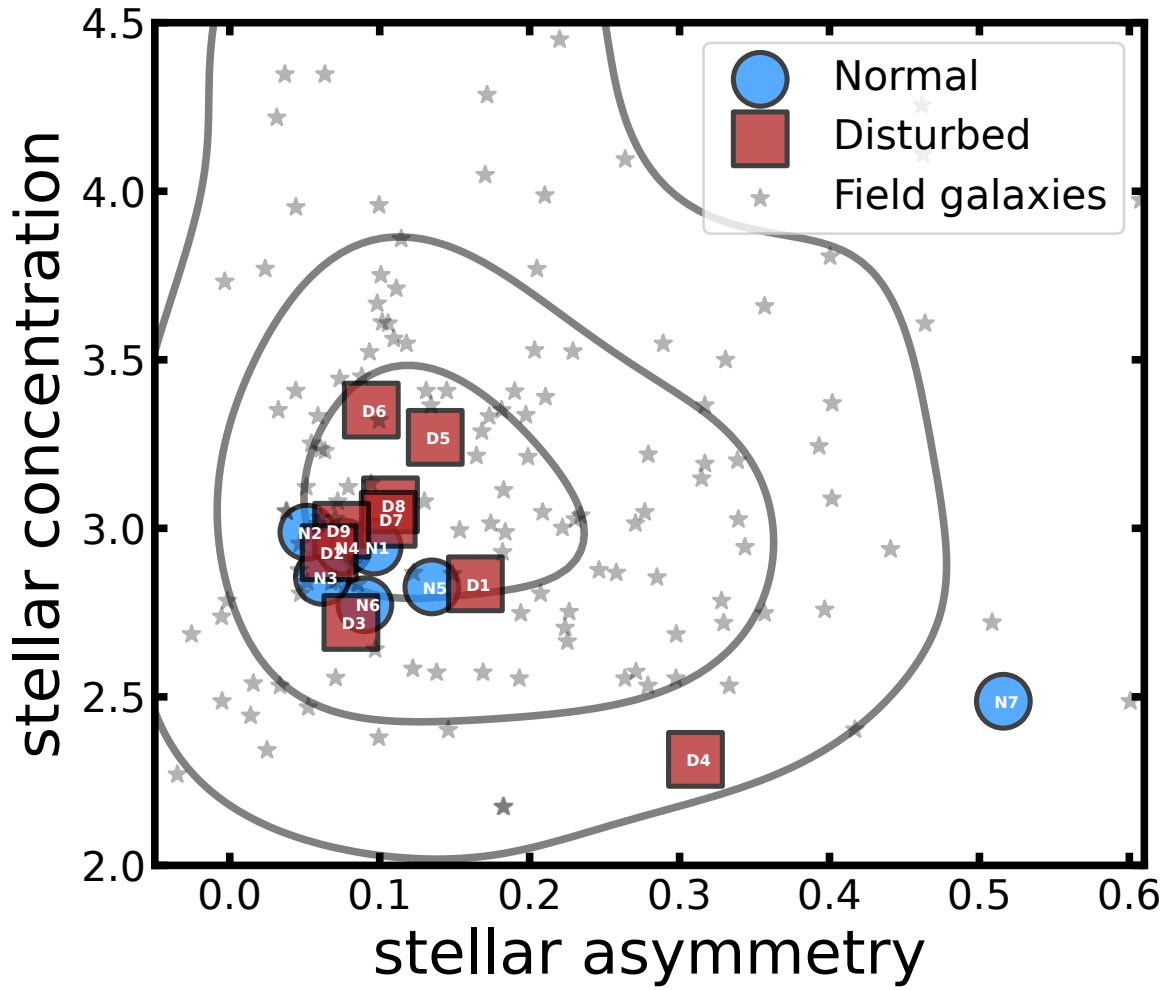


Figure S5: The concentration vs asymmetry plane for cluster members. The backgrounds grey stars are field galaxies at the same redshift and the corresponding contours show their cumulative distribution at 16%, 50% and 84% levels.

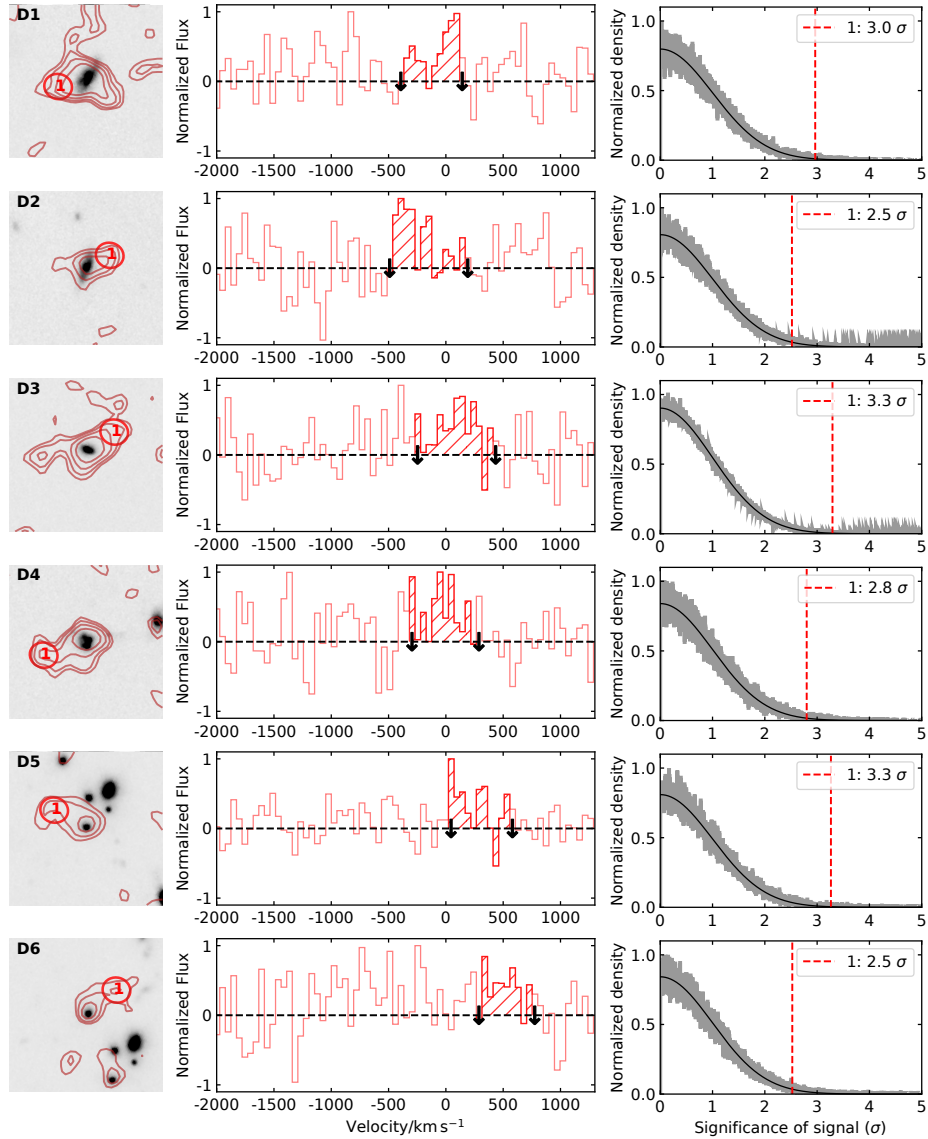


Figure S6: The significance of the detections of extended structures in the disturbed galaxies.

From left to right: *Left:* The CO(3-2) moment-0 maps (red) contoured on the JWST F444W image. The contours level as $[\sqrt{2}, 2, 2\sqrt{2}, 4, 8, 16]\sigma$. The ellipses denote the interested extended structures. *Middle:* The mean spectrum from the ellipses in the left panel. The arrows show the line widths in the host galaxies. *Right:* The significance of detections within the ellipses marked in vertical dashed lines. The grey histogram is the noise distribution and the black solid lines are the best-fitted Gaussian model.

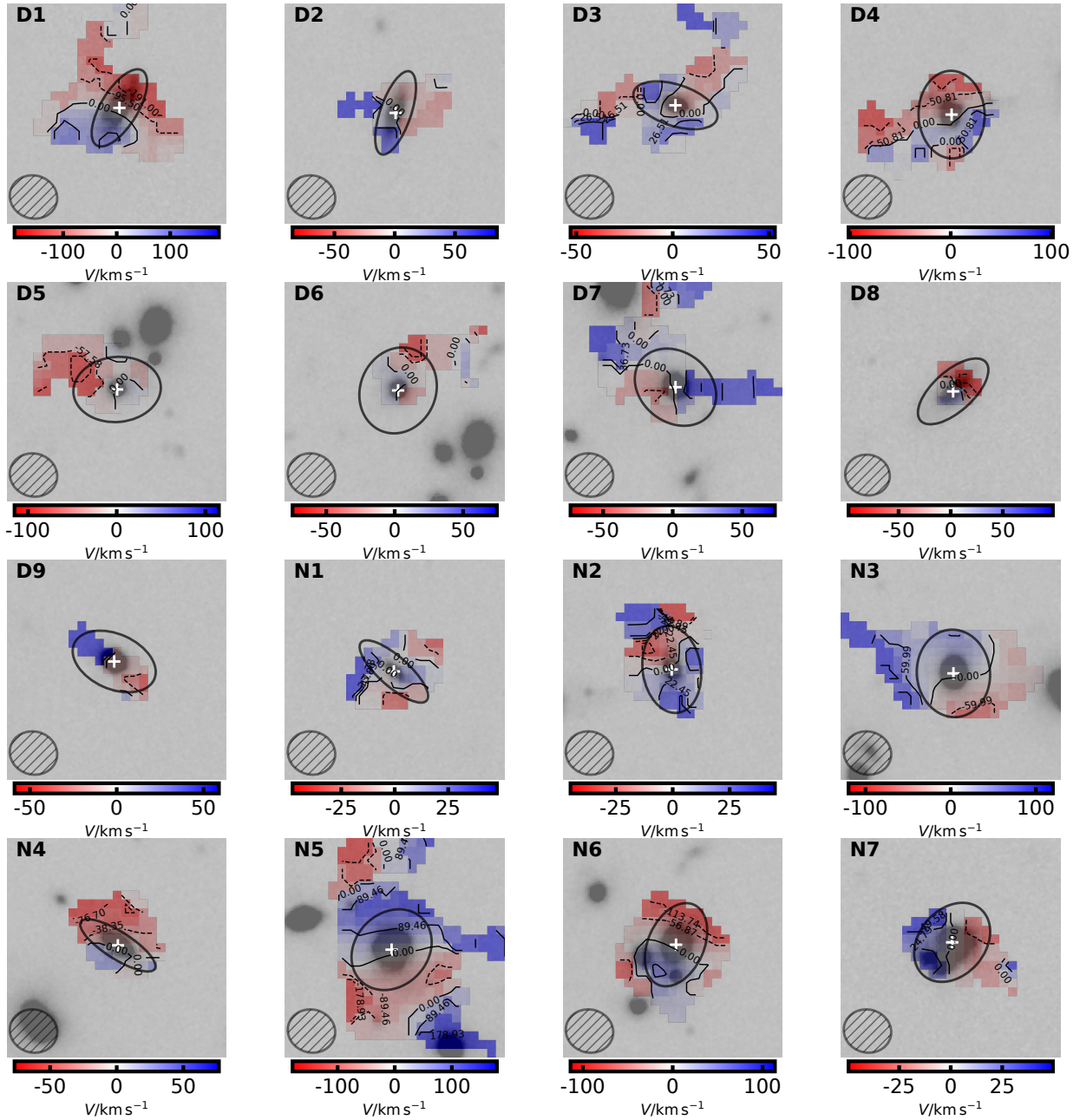


Figure S7: The velocity distribution on the F444W images for the CO(3-2) detected cluster member galaxies. In each panel, we show the moment-1 maps for the normal and disturbed galaxies. The lower left ellipse denotes the synthesized beam size of ALMA observation and galaxy IDs are labeled in the upper left. The black ellipses at center denote the shapes of the stellar component from PETROFIT. The contours and the inline numbers show the velocity gradient.

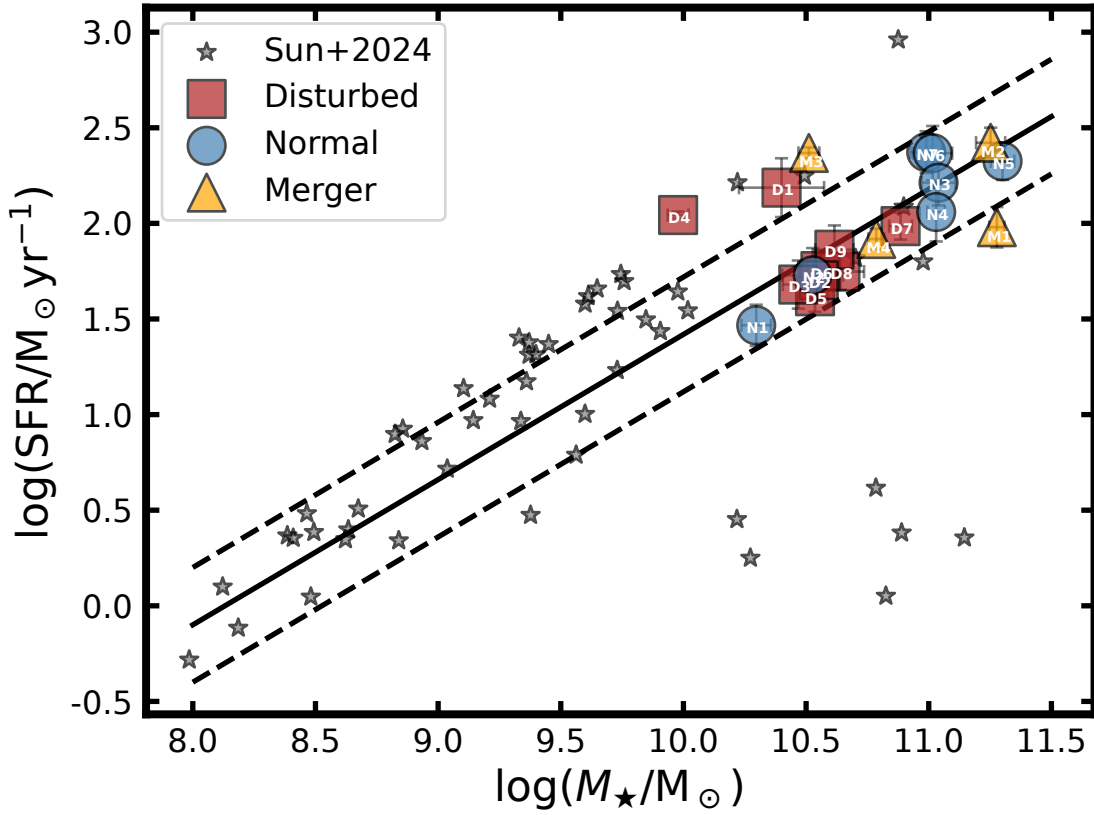


Figure S8: The plot between SFR and M_{\star} for cluster members. The star-formation main sequence is adopted from ref. (25, 60), and the dashed lines denote the 0.3 dex offset from the main sequence. The background grey stars are the cluster member galaxies selected in ref. (6). The error bars show 1σ standard deviation.